A new meridian imaging spectrograph for the auroral spectroscopy

Makoto Taguchi[1], Shoichi Okano[2], Takeshi Sakanoi[2],
Naoko Koizumi[2], Takehiko Aso[1] and Masaki Ejiri[1]

[1]National Institute of Polar Research, Kaga 1-chome, Itabashi-ku, Tokyo 173-8515
[2]Planetary Plasma and Atmospheric Research Center, Tohoku University,
Aoba, Aramaki, Aoba-ku, Sendai 980-8578

Abstract: Spectroscopic and monochromatic imaging observations of emissions in the upper atmosphere are mutually complementary. A meridian imaging auroral spectrograph (ASG) that can measure a spectrum in the visible region along a meridian has been developed for research on the auroral physics and the polar upper-atmosphere dynamics. Combination of a fast optical system inherited from a monochromatic all-sky imager, a grism as a dispersive element, and a cooled CCD camera has enabled a wide field-of-view of 180° along a meridian, spectral coverage of 420–730 nm, spectral resolution of 1.5–2.0 nm, and high sensitivity to be obtained. The absolute sensitivity over a full-image field was calibrated using a National Institute of Standards and Technology (NIST) traceable integrating sphere and determined to be 0.06 cts/s/R at a wavelength of 560 nm at the zenith. The ASG was installed at Longyearbyen in March 2000, and routine operation was started in the 2000/2001 winter season. An example of an auroral spectral image is presented in this report to demonstrate the performance of the ASG.

1. Introduction

Spectroscopic investigations have provided significant information on the sources and mechanism of auroral emissions, energy distribution and the flux of auroral particles, and the chemical and dynamical conditions of the upper atmosphere (*e.g.*, Rees *et al.*, 1976; Deehr *et al.*, 1980; Paresce *et al.*, 1983; Ishimoto *et al.*, 1988; Rassoul *et al.*, 1993; Stephan *et al.*, 2001). On the other hand, optical imaging observations, both from the ground and from space platforms, have been a basic approach to researches on the auroral physics, the auroral substorm dynamics, and the mapping of auroral particles, etc. (*e.g.*, Akasofu, 1964; Anger *et al.*, 1973, 1987; Ono *et al.*, 1987; Frank and Craven, 1988; Oguti *et al.*, 1990; Newell *et al.*, 1992; Tobiska *et al.*, 1993; Evans *et al.*, 1994; Cummer *et al.*, 2000). Use of highly sensitive CCD devices has drastically improved the sensitivity and time resolution of imaging instruments promoting studies on gravity wave propagations deduced from the patterns seen in successive images of faint airglow (*e.g.*, Mendillo *et al.*, 1997; Taylor *et al.*, 1995). Recently, Rees *et al.* (2000) succeeded in obtaining an optical image of the visible aurora under near-daytime conditions using a high-resolution imaging optical spectrometer.

An optical instrument combining spectroscopy and imaging techniques makes it possible to investigate the spatial distribution and motion of spectroscopic phenomena, such as aurora and airglow. Grating spectrographs, which are capable of taking an image whose ordinate and abscissa are projections of a slit and wavelength, respectively, have been developed for this purpose. Okamura and Ejiri (1992) applied this technique to auroral observations and studied the differences in the horizontal distribution and the temporal variation of auroral emissions. Swenson *et al.* (1998) also discussed the vertical profiles of auroral emissions in the visible and near-IR regions using data acquired by an imaging spectrograph. Semeter *et al.* (1999) analyzed auroral spectroscopic data obtained by a chain of meridional imaging spectrographs to reconstruct an emission field by a tomographic method. Chakrabarti *et al.* (2001) presented a unique imaging spectrograph with high-spectral resolution and high throughput for ground-based observations of airglow and aurora; they described the performance of the instrument in both laboratory and field experiments. Dymond *et al.* (2000) developed an ultraviolet spectrograph for a sounding rocket experiment which gives height profiles of O and O_2 densities from spectral images obtained during a rocket flight.

The National Institute of Polar Research, Japan, has developed a monochromatic all-sky imager (ASI) with high sensitivity and high time resolution for studies on aurora and airglow phenomena (Okada *et al.*, 1997). An ASI has been in operation at the South Pole Station since the 1997 austral winter season; two additional ASIs were installed at Syowa Station in 1998. One of the ASIs at Syowa Station was brought back to Japan in 1999 and modified to become an imaging auroral spectrograph (ASG) so that spectral images of aurora and airglow can be obtained. In this paper, we describe instrumentation and performance of the ASG and present example data obtained from observations at Longyearbyen to demonstrate its actual performance.

2. New auroral spectrograph

The performance requirements of the ASG are: 1) a field-of-view that covers the entire meridian, 2) spectral resolution of higher than 2 nm, 3) spectral coverage over the full-range of the visible region, and 4) sensitivity comparable to that of the ASI. Satisfying all of these requirements using a conventional optical layout with a diffraction grating is quite difficult. However, a grism or a transmission grating grooved on a prism surface can be used as a compact dispersive element with both high throughput and moderate spectral resolution, because the light diffracted by a grism does not overlap the path of the incident light. Thus, a grism was used as the dispersive element in the ASG. The main specifications of the ASG are listed in Table 1.

The optical layout illustrated in Fig. 1 is similar to that used in the ASI with the exception that a grism is used as the dispersive element in place of the ASI's interference filter. The optical system is composed of a fast fish-eye lens ($f = 6$ mm, F1.4), a collimator lens system, a grism, and an imaging lens system. The grism is inserted at the position where the ray becomes parallel. The grooved surface of the grism faces the fore-optics. The optical axis of the fore-optics is normal to the grooved surface. A slit with a width of 42 μm and a length of 20 mm is placed at the focal plane of the fish-eye lens.

A groove frequency of 600 gr/mm and a BK7 glass material were chosen so that the

Table 1.   Specifications of the auroral spectrograph.

|	
Optical front-end	Fish-eye lens 6 mm F1.4
Slit width	42 μm
Grism	
Dimension	68 mm × 68 mm
Blank material	BK7
Groove frequency	600 g/mm
Blaze wavelength	450 nm
Prism angle	26.75°
CCD	
Number of pixels	512 × 512
Pixel size	24 μm
Quantum efficiency	>80% in visible region
Temperature	−40°C
Spectral region	420–730 nm
Spectral resolution	1.5 nm @ 550 nm
Field-of-view	180°
Spatial resolution	0.37–0.98°
Sensitivity	0.062 cts/s/R @ 550 nm
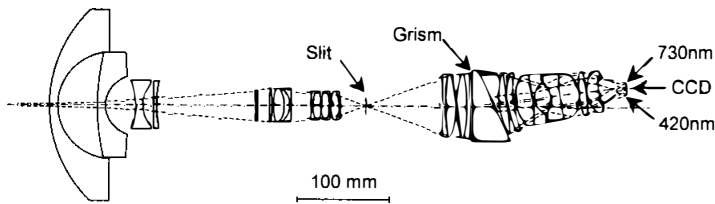
Fig. 1.   Optics of the ASG.   The optical paths are projected on a plane including the optical axes of the fore optics and the focusing optics.   The meridional plane is perpendicular to this plane.

dispersed wavelength range of interest falls just inside the sensitive area of a CCD detector. Both surfaces of the grism are AR-coated.   The efficiency of the grism ranges from 40% at 730 nm to more than 75% at 450 nm.   These efficiencies are comparable to the peak transmission of the interference filters used in the ASIs for selection of auroral emission lines.   Accordingly, the ASG is expected to have high sensitivity that is almost equivalent to that of the ASI.   The prism, which contributes in part to the wavelength dispersion, functions as a beam-stirring optical component to minimize the angle between the optical axes of the fore-optics and the focusing optics.

A back-thinned bare CCD (512 by 512 pixels) can take images in a form such that the zenith angle and wavelength are aligned along the rows and lines of the CCD, respectively.   The CCD is cooled down to a temperature lower than −40°C using a three-stage Peltier cooler to minimize dark noise.   The pixel size of 24 μm matches the monochromatic images produced by the slit's width.   Along the meridian, the CCD resolves a 180° field-of-view into approximately 500 pixels, making the spatial resolution along the meridian about 0.36°.   The position and tilt of the CCD can be adjusted and fixed by small set-screws.   These mechanisms make tuning of the spectral coverage and focusing easier.

Charges accumulated by the CCD are amplified and converted to 14-bit digital signals, which are processed by a computer and stored in a DVD-RAM disk. The preamplifier's gain can be selected as either a super high gain (6 e$^-$/bit), a high gain (30 e$^-$/bit), or a low gain (60 e$^-$/bit). The gain is normally set at a super high gain, but a high or low gain can be selected when a high signal-to-noise ratio and a wide dynamic range are required for bright auroras.

3. Calibration

3.1. Spatial resolution

The spatial resolution across the meridian was experimentally determined as follows. A rail was placed in such a way that the rail was perpendicular to a plane containing the field-of-view of the ASG. Images of a small spectral lamp, which could be moved along the rail, were taken by changing the position of the lamp in small steps across the field-of-view. The distance between the lamp and the fish-eye lens was set at 3.1 m so that the angle subtended by the emitting area of the lamp at the fish-eye lens was much smaller than the field-of-view expected from the distance between the ASG and the lamp and a CCD pixel size. The results are shown in Table 2. The spatial resolution near the horizon, 0.37°, is close to the originally designed value of 0.36° near the zenith, the spatial resolution became 0.98°.

Table 2. *Spatial resolution of the ASG.*

Zenith angle	Resolution
90°	0.37°
0°	0.98°
−90°	0.37°

In general, spatial resolution at the outer field-of-view of an optical component tends to be worse than that at the inner field-of-view because of aberrations. However, our experimental results show the opposite findings. The causes of the variation in spatial resolution have not been clarified, but mechanical distortion of the thin slit plate ($t = 20$ μm) is suspected to be partially responsible. Since the slit plate is held in place by a ring with a diameter of $\sim$20 mm, the outer part of the slit plate can be fixed in the focal plane. If the plate is not sufficiently rigid, however, the central part might be slightly out of the focal plane. A similar effect can occur, if the focal plane is curved.

3.2. Spectral range and resolution

The spectral range and resolution were measured using images of an integrating sphere illuminated by three spectral calibration lamps (Hg, Kr or Ne), and a He-Ne laser. The integrating sphere of the National Institute of Polar Research, Japan serves as an ideal isotropic light source, because it has a large spherical cavity, 2 m in diameter, whish is sufficient for the calibration of almost any kind of all-sky optics. Figure 2 shows a raw image of the integrating sphere illuminated by a Hg lamp. In addition to a dominant spectral line at 546.1 nm, two adjacent spectral lines of Hg at 577.0 and 579.1 nm and a weak spectral line at 435.8 nm can be clearly identified. The slight curvature of the
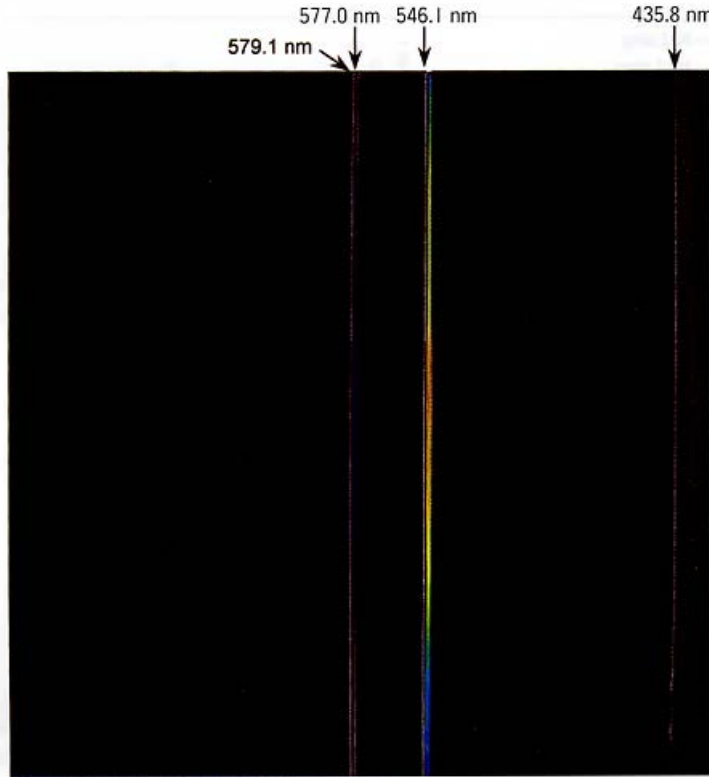
Fig. 2. *A raw image of the integrating sphere illuminated by a Hg lamp without any correction. The intensity is scaled using a pseudo-false color code   North and violet are to the top and right of the image, respectively.*

spectral lines is caused by the difference in incident angles to the grism between $0°$ for the beam from the zenith and about $5.6°$ for the beam from the horizon.

The spectra of the spectral calibration lamps and a He-Ne laser at zenith angles of $0°$, $+45°$ and $+90°$ are shown in Fig. 3. The measured spectral range was determined from the positions of the isolated dominant spectral lines whose wavelengths are known. The range always covers 420–730 nm. The full range shifts slightly towards longer wavelengths as the zenith angle increases   Since the glasses used in the ASG optics are not transparent for light with wavelengths shorter than 370 nm, the observed spectrum is free from contamination by higher order spectra.

From these spectral line profiles, the FWHMs of the major spectral lines Hg 546.1 nm. Kr 557.0 and 587.1 nm and He-Ne 632.8 nm were measured to be about 1.7 nm. In addition, the adjacent spectral lines of Hg at 577.0 nm and 579.1 nm were completely resolved. Therefore, the spectral resolution was conservatively estimated to be 2 nm.

To evaluate the limit of the spectral resolution more quantitatively, we performed simulations in which two identical spectral line profiles, which are equivalent to those actually measured by the ASG, are superimposed by changing the separation between their positions by multiples of ΔX which is the resolution calculated simply from the wave-
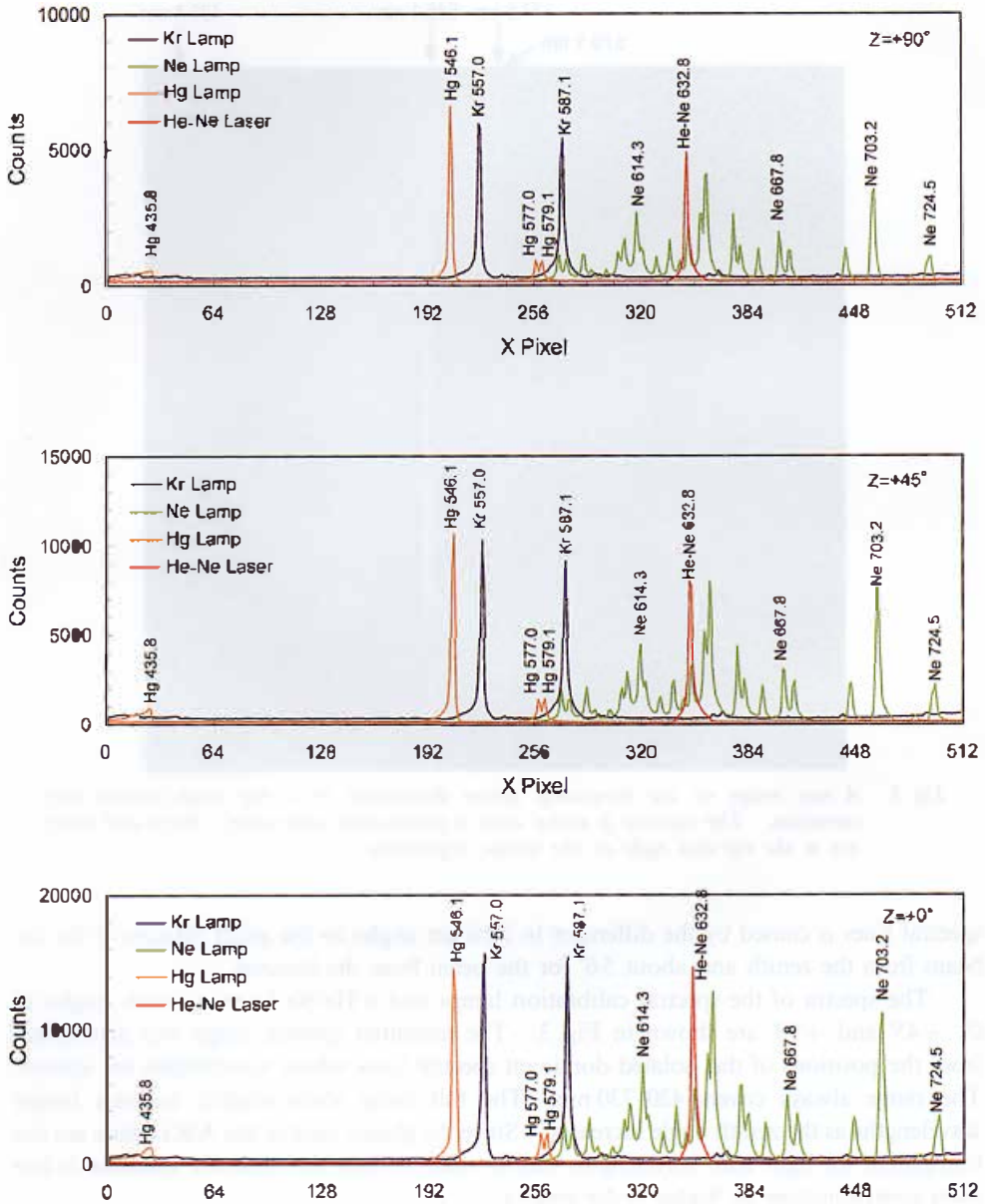
Fig. 3.   Spectra of the spectral calibration lamps and laser extracted from the image data
shown in Fig 2 at zenith angles (Z) of 0°, +45°, and +90°.

length dispersion, the focal length of the imaging optics, and the CCD pixel size, as shown in Fig. 4.   In most of the simulation results, the spectral lines were not resolved when they were separated by two ΔXs, e.g., 1.2 nm, however, a distinct minimum between the two peaks was clearly seen when the separation was three ΔXs, e.g., 1.8 nm.   Consequently, the spectral resolution is estimated to be 1.5 nm for wavelengths between 540 and 650 nm.
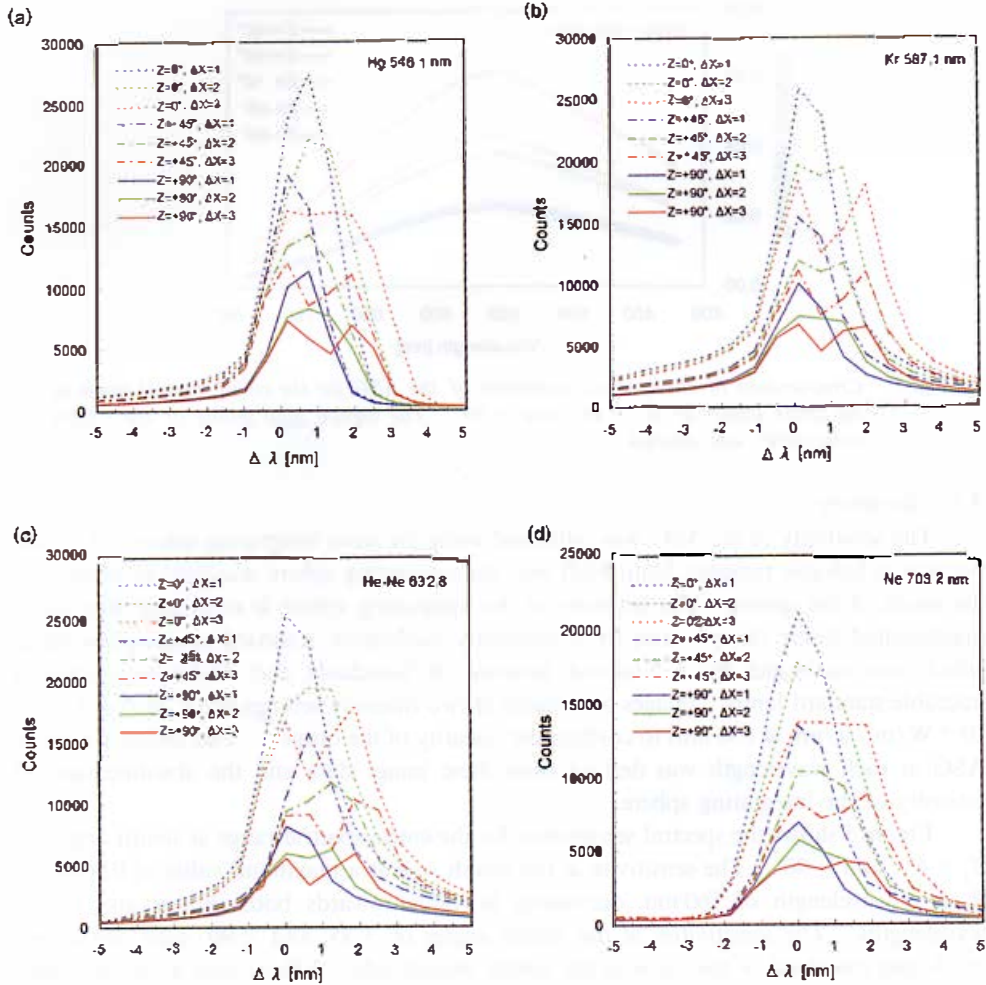
Fig. 4. Simulations in which an actually measured spectral emission line is superimposed on itself after being shifted by one, two or three ΔXs to indicate how the ASG resolves two adjacent spectral lines. The spectral lines of a) Hg 546.1 nm, b) Kr 587.1 nm, c) He-Ne 632.8 nm, and d) Ne 703.2 nm shown in Fig. 3 were selected for these simulations. One ΔX corresponds to a wavelength difference of about 0.6 nm. For each spectral line, nine combination of zenith angles (0°, +45°, and +90°) and one, two, and three ΔXs are plotted.

The spectral resolution decreases to about 2.0 nm near the shorter and longer wavelength limits as a result of aberration of the overall optics.

A comparison of the spectra at different zenith angles indicates that the spectral resolution has no clear dependence on the zenith angle. Note that the spectral resolution of the ASG can be improved by a factor of two, if the width of the slit is halved and the CCD is replaced by one with 1000 by 1000 12 μm pixels.

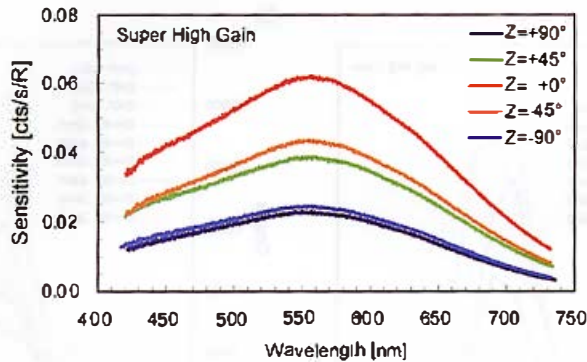Fig. 5. *Cross-sections of the spectral sensitivities of the ASG for the entire spectral range at the zenith angles of 0°, ±45°, and ±90°. The highest gain setting of the CCD's preamplifier was selected.*

3.3. Sensitivity

The sensitivity of the ASG was calibrated using the same integrating sphere.   For this purpose, a halogen tungsten lamp built into the integrating sphere was used to illuminate the inside of the sphere.   The intensity of the integrating sphere is calibrated after every one-hundred hours of operation by a secondary calibration standard spectrophotometer which was calibrated by a National Institute of Standards and Technology (NIST) traceable standard lamp.   Images were taken at two intensity settings (0.5×10^{-4} and 1.0×10^{-4} W/m^2/sr/nm at 630 nm) to confirm the linearity of the output.   The sensitivity of the ASG at each wavelength was derived from these image data and the absolute spectral intensity of the integrating sphere.

Figure 5 shows the spectral sensitivities for the entire spectral range at zenith angles of 0°, ±45°, and ±90°.   The sensitivity at the zenith was at a maximum value of 0.06 cts/s/R at a wavelength of 560 nm, decreasing in value towards both shorter and longer wavelengths.   The sensitivities at the zenith angles of ±45° and ±90° were about two thirds and one third of the value at the zenith, respectively.   Effects such as the efficiency of the grism, vignetting of the optics, and the spectral response of the CCD are thought to produce the wavelength and zenith angle dependences of the spectral sensitivity.

4. Example of auroral spectrum

The ASG was installed at Longyearbyen, Spitzbergen in March 2000, and observations were started in the 2000/2001 winter season.   Images of auroral spectra along the geomagnetic meridian were recorded every three minutes with an exposure time of 15 s. Figure 6 shows an example of an auroral spectral image obtained in the morning on December 6, 2000.   The sky was clear at the time of observation.   The emission intensities have been calibrated, and the spectral line distortion due to difference in incident angles to the grism has been corrected.   Note that the observed wavelength region, 450–765 nm, has been slightly shifted towards a longer wavelength, compared with the range obtained when the ASG was calibrated in Japan.

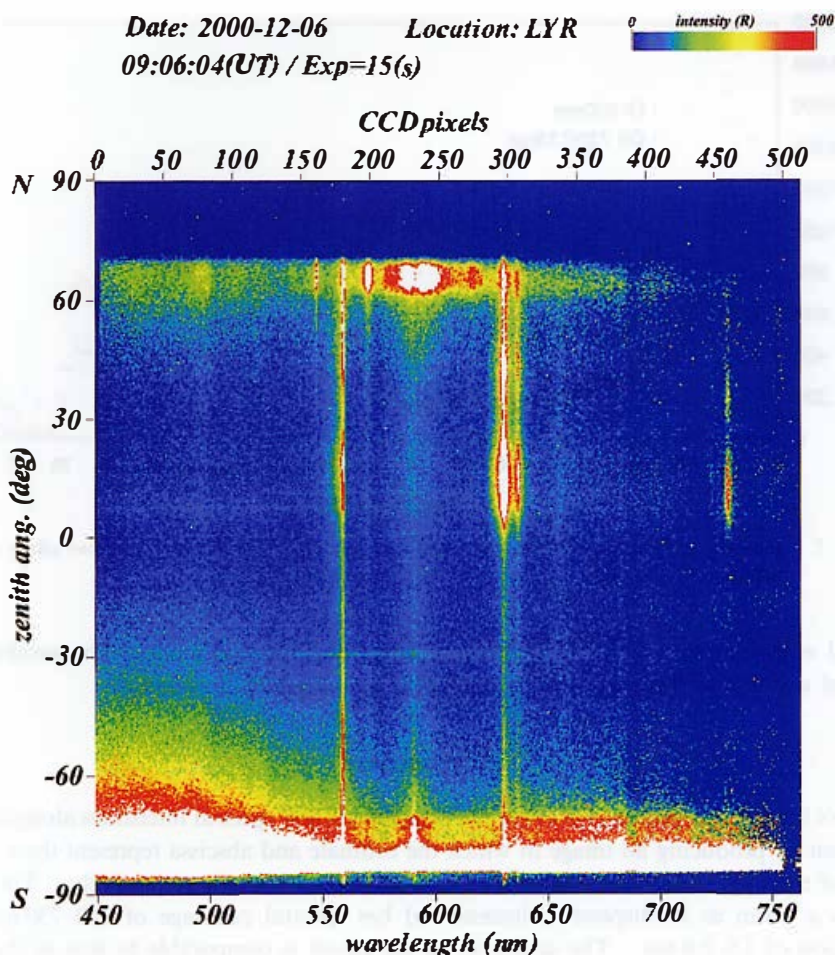The field-of-view of the ASG up to about 20° above the northern horizon is blocked

Fig. 6. An auroral spectrum image obtained by the ASG at Longyearbyen on December 6, 2000.

by a nearby building. The southern horizon was illuminated by twilight. Dominant auroral emission lines, such as OI 557.7, 630.0, and 636.4 nm and OII 732/733 nm, are apparent in the northern sky. A strong NaD line emission (589 nm) due to city light contamination is also seen in the low northern sky.

From the data shown in Fig. 6 the intensity distributions of the OI 630.0 nm and OII 732/733 nm emissions along the meridian were plotted in Fig 7. In the northern sky the profiles of both the OI 630.0 nm and OII 732/733 nm emissions have a similar pattern with three distinct peaks, but the peaks of the OII 732/733 nm emission are located at a slightly higher elevation compared with the peaks of the OI 630.0 nm emission. This indicates that three discrete auroras, in which the altitude regions of ion emissions were higher than those of neutrals, overlapped along the line-of-sight direction of the ASG. To obtain the actual altitude profiles of the emissions, the horizontal distance between the observatory and the auroral arcs must be known, or some assumptions on the altitude of characteristic
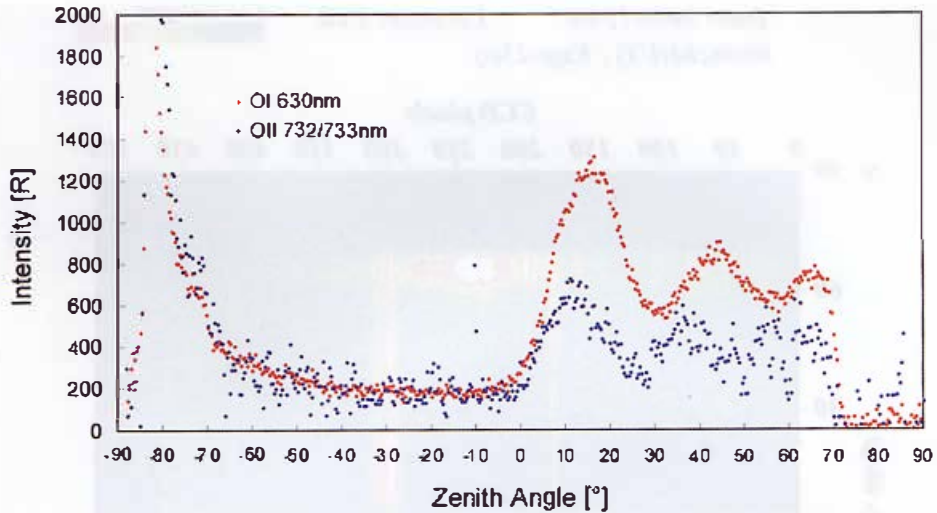
Fig. 7.   Intensity distributions of the OI 630.0 nm and OII 732/733 nm emissions along the
meridian.   The data are same as those shown in Fig. 6.

auroral emission, such as the OI 557.7 nm emission, must be made.   The results of a
detailed analysis of these emission profiles will be presented elsewhere.

5. Summary

We have developed an ASG that can measure auroral spectral intensities along the full
meridian by producing an image in which the ordinate and abscissa represent the a zenith
angle of the meridional field-of-view and the spectral wavelength, respectively.   The ASG
utilizes a grism as its dispersive element and has spectral coverage of 420–730 nm and
resolution of 1.5–2.0 nm.   The sensitivity at the zenith is comparable to that of the ASI,
though the sensitivity at the horizon decreases to about one third of the value at the zenith.
The ASG was installed at Longyearbyen in March 2000, and observations were started in
the 2000/2001 winter season.   An example of a fully corrected and calibrated auroral
spectral image is presented.

References

Akasofu, S.-I. (1964): The development of the auroral substorm.   Planet. Space Sci., 12, 273–282.

Anger, C.D., Fancott, T., McNally, J. and Kerr, H.S. (1973): ISIS-II scanning auroral photometer. Appl. Opt., **12**, 1753–1766.

Anger, C.D., Murphree, J.S., Vallance Jones, A., King, R.A., Broadfoot, A.L., Cogger, L.L., Creutzberg, F., Gattinger, R.L., Gustafsson, G., Harris, F.R., Haslett, J.W., Llewellyn, E.J., McConnell, J. C., McEwen, D.J., Richardson, E.H., Rostoker, G., Sandel, B.R., Shepherd, G.G., Venkatesan, D., Wallis, D.D. and Witt, G. (1987): Scientific results from the Viking ultraviolet imager: an introduction. Geophys. Res. Lett., **14**, 383–386.

Chakrabarti, S., Pallamraju, D. and Baumgardner, J. (2001): HiTIES: A High Throughput Imaging Echelle Spectrograph for ground-based visible airglow and auroral studies. J. Geophys. Res., **106**, 30337–30348.

Cummer, S.A., Vondrak, R.R., Ostgaard, N., Stadsnes, J., Bjordal, J., Chenette, D. L., Brittnacher, M.J., Parks, G.K., Sigwarth, J.B. and Frank L.A. (2000): Global multispectral auroral imaging of an isolated substorm. Geophys. Res. Lett., **27**, 637–640.

Deehr, C.S., Sivjee, G.G., Egeland, A., Henriksen, K., Sandholt, P.E., Smith, R., Sweeney, P., Duncan, C. and Gilmer, J. (1980): Ground-based observations of F region aurora associated with the magnetospheric cusp. J. Geophys. Res., **85**, 2185–2192.

Dymond, K.F., McCoy, R.P., Thonnard, S.E., Budzien, S.A., Thomas, R.J., Bullett, T.N. and Bucsela, E.J. (2000): O$^+$, O, and O$_2$ densities derived from measurements made by the High Resolution Airglow/Aurora Spectrograph (HIRAAS) sounding rocket experiment. J. Geophys. Res., **105**, 23025 23033.

Evans, J.S., Strickland, D.J., Anderson, D.E., Jr., Conway, R.R., Smathers, H.W., Bakeris, D.F., Swanson, R.A., Chubb, T. A. and Cardon, J.G. (1994): Ultraviolet plume instrument imaging from the LACE satellite: Analysis of broadband UV auroral limb data. J. Geophys. Res., **99**, 17591–17600.

Frank, L.A. and Craven, J.D. (1988): Imaging results from Dynamics Explorer I. Rev. Geophys., **26**, 249–283.

Ishimoto, M., Meng, C.-I., Romick, G.J. and Huffman, R.E. (1988): Auroral electron energy and flux from molecular nitrogen ultraviolet emissions observed by the S3-4 satellite. J. Geophys. Res., **93**, 9854–9866.

Mendillo, M., Baumgardner, J., Nottingham, D., Aarons, J., Reinisch, B., Scali, J. and Kelly, M. (1997): Investigations of thermospheric-ionospheric dynamics with 6300-Å images from the Arecibo Observatory. J. Geophys. Res., **102**, 7331–7343.

Newell, P.T., Meng, C.-I. and Huffman, R.E. (1992): Determining the source region of auroral emissions in the prenoon oval using coordinated Polar BEAR UV-imaging and DMSP particle measurements. J. Geophys. Res., **97**, 12245 12252.

Oguti, T., Kaneda, E., Ejiri, M., Sasaki, S., Kadokura, A., Yamamoto, T., Hayashi, K., Fujii, R. and Makita, K. (1990): Studies of aurora dynamics by auroral-TV on the Akebono (EXOS-D) Satellite. J. Geomag. Geoelectr., **42**, 555–564.

Okada, M., Ejiri, M., Okano, S., Taguchi, M., and Takeshita, S. (1997): System design and initial results of all sky imager at South Pole, Nankyoku Shiryô (Antarctic Record), **41**, 613–630.

Okamura, H. and Ejiri, M. (1992): A new imaging spectrometer for the auroral spectroscopic studies. J. Geomag. Geoelectr., **44**, 193–205.

Ono, T., Ejiri, M. and Hirasawa, T. (1987): Monochromatic auroral images observed at Syowa Station, in Antarctica. J. Geomag. Geoelectr., **39**, 65–95.

Paresce, F., Chakrabarti, S., Kimble, R. and Bowyer, S. (1983): The 300- to 900-Å spectrum of a nightside aurora. J. Geophys. Res., **88**, 10247–10252.

Rassoul, H.K., Rohrbaugh, R.P., Tinsley B.A. and Slater, D.W. (1993): Spectrometric and photometric observations of low-latitude aurorae. J. Geophys. Res., **98**, 7695–7709.

Rees, D., Conde, M., Steen, Å. and Brändström, U. (2000): The first daytime ground-based optical image of the aurora. Geophys. Res. Lett., **27**, 313–316.

Rees, M.H., Sivjee, G.G. and Dick, K.A. (1976): Studies of molecular nitrogen bands from airborne auroral spectroscopy. J. Geophys. Res., **81**, 6046 6058.

Semeter, J., Mendillo, M. and Baumgardner, J. (1999): Multispectral tomographic imaging of the midlatitude aurora. J. Geophys. Res., **104**, 24565–24585.

Stephan, A.W., Chakrabarti, S., Dymond, K.F., Budzien, S.A., Thonnard, S.E. and McCoy, R.P. (2001):

Far ultraviolet equatorial aurora during geomagnetic storms as observed by the Low-Resolution Airglow and Aurora Spectrograph. J. Geophys. Res., **106**, 30323–30330.

Swenson, G.R., Rairden, R.L., Solomon, S.C. and Ananth, S. (1998): Imaging spectroscopy for two-dimensional characterization of auroral emissions. Appl. Opt., **37**, 5760–5770.

Taylor, M.J., Fritts, D.C. and Isler, J.R. (1995): Determination of horizontal and vertical structure of an unusual pattern of short period gravity waves imaged during ALOHA-93. Geophys. Res. Lett., **22**, 2837–2840.

Tobiska, W.K., Gladstone, G.R., Chakrabarti, S., Shepherd, M.G., McConnell, J.C., Link, R., Schmidtke, G. and Stasek, G. (1993): FUV-visible photometric imaging of aurorae. J. Geophys. Res., **98**, 17525–17535.